INORGANIC CHEMISTRY FRONTIERS

RESEARCH ARTICLE

View Article Online
View Journal | View Issue

Cite this: *Inorg. Chem. Front.*, 2025, **12**, 261

Water-stable perovskite nanotube array with enhanced transport of charge carriers induced by functionalized polyoxometalate for the highly efficient photoreduction of uranium(VI)†

Yanli Yang,‡[a] Keke Guo,‡[a,b] Xue Bai,[a] Maochun Zhu,[a] Siyue Wang[a] and Shuxia Liu *[a]

Since metal halide perovskites (MHPs) possess excellent optoelectronic performances, constructing MHP-based photocatalysts is a promising strategy to promote photocatalytic uranium(VI) reduction. However, the instability of MHPs in water limits their practical application, which is still a major issue and challenge. In this work, we constructed a perovskite nanotube array-based catalyst encapsulated by a functionalized POM, $(HMTA)_3Pb_2Br_7$@STA-PW_{12}, which can maintain stability in water for 10 hours under stirring conditions. It is noteworthy that considering the "electron-sponge" property of POMs, STA-PW_{12} acting as an electronic transfer medium not only increases the stability of the catalyst in water due to the hydrophobic long-chain STA but also contributes to the separation of photogenerated carriers and enhances charge transfer from $(HMTA)_3Pb_2Br_7$ to PW_{12}, which significantly enhances the photocatalytic activity. The enhanced electron carrier mobility (μ_e) (1.1 $cm^2\ V^{-1}\ s^{-1}$) and carrier diffusion length (245 nm) of $(HMTA)_3Pb_2Br_7$@STA-PW_{12} further illustrate its effective charge carrier transfer. DFT calculations further indicate the transition of electrons from $(HMTA)_3Pb_2Br_7$ to PW_{12}, which greatly inhibits the recombination of photogenerated carriers, thereby advancing electron transfer. Finally, the synthesized catalyst exhibits an excellent performance in the photocatalytic removal of U(VI) with a removal rate of 99.3% at a U(VI) concentration of 40 ppm after 40 min under simulated sunlight.

Received 20th September 2024,
Accepted 8th November 2024

DOI: 10.1039/d4qi02393e

rsc.li/frontiers-inorganic

Introduction

Nuclear power is the energy of the future owing to its inherent merits of low carbon emissions, high power densities, and low power generation costs.[1–4] Uranium is one of the essential components in nuclear fuel and can be easily released into the environment during nuclear activities.[5–7] In radioactive wastewater, uranium exists in the form of stable and dissolved U(VI), which possesses the characteristics of strong migration capacity and chemical toxicity. It can cause serious harm to the ecosystem and human beings if it enters the natural environment through natural infiltration and water migration.[8–11] Therefore, effectively removing U(VI) from uranium-containing wastewater is an issue that needs to be solved. In recent years, reducing soluble U(VI) to insoluble U(IV) using photocatalytic technology, which have the advantages of possessing extensive energy sources and sustainable development, has provided a new approach for treating uranium-containing wastewater.[12–15] For instance, in 2019, Wang *et al.* designed and synthesized a polyoxometalate (POM)–organic framework material (SCU-19), which exhibits advanced removal performance toward U(VI) radionuclides under visible light irradiation.[16] In 2024, Yu *et al.* reported a TTh-COF-TiO_2 catalyst, which shows a superior U(VI) removal rate of 99.8% within 40 min under visible light irradiation.[17] In the photocatalytic reaction system, solar-driven energy conversion is a promising technology for a sustainable energy future and environmental remediation. An efficient catalyst with effective separation of photogenerated electron–hole pairs and electron transfer is the key to further improve the efficiency of U(VI) reduction.

Over the past decade, metal halide perovskites (MHPs) have triggered interdisciplinary interest and revolutionized optoelectronic fields due to their fantastic properties, such as

[a]*Key Laboratory of Polyoxometalate and Reticular Material Chemistry of Ministry of Education, Faculty of Chemistry, Northeast Normal University, Changchun, Jilin 130024, P. R. China. E-mail: liusx@nenu.edu.cn*
[b]*Key Laboratory of Eco-Functional Polymer Materials of the Ministry of Education, College of Chemistry and Chemical Engineering, Northwest Normal University, Lanzhou, Gansu 730070, P.R. China*

†Electronic supplementary information (ESI) available. See DOI: https://doi.org/10.1039/d4qi02393e

‡These authors contributed equally to this work.

broad light absorption range, high charge mobility, long carrier diffusion length, and low-cost solution processing.[18–21] Inspired by these merits, the utilization of MHPs for solar-to-chemical energy conversion has also gained much attention in recent years, especially in the field of photocatalysis. Since the first work reported by Park *et al.* in 2016, who used $CH_3NH_3PbI_3$ ($MAPbI_3$) as a photocatalyst for H_2 generation,[22] MHPs have been successfully adopted for photocatalytic H_2 evolution, organic synthesis, CO_2 reduction and pollutant degradation.[23–25] Despite these encouraging achievements, their stability issue has been considered the main bottleneck that limits their further applications, especially their instability against water since most MHPs are very sensitive to water and tend to be degraded rapidly when in contact with water molecules. To improve the stability of MHPs in aqueous media, some strategies modifying MHPs with water-proof material have been recently developed, such as designing a core–shell structure, crafting functional layers, and constructing encapsulation layers to screen the MHPs from water molecules.[26–28] For instance, in 2019, Lu *et al.* encapsulated $MAPbI_3$ perovskite quantum dots (QDs) in the pores of metal–organic framework (MOF) PCN-221(Fe_x) to construct a series of composite photocatalysts of $MAPbI_3$@PCN-221(Fe_x) (x = 0–1), which exhibits an excellent performance for photocatalytic CO_2 reduction using water as an electron source.[29] However, as shown in Scheme 1, although modifying MHPs with water-proof material can enhance their stability in water, characteristics of these materials being insensitive to electrons may hinder the transfer of photogenerated carriers, which is not conducive to the progress of the reaction. Thus, we believe that constructing MHPs composite catalyst modified by water-proof materials combining media with excellent electronic transfer capability may promote the charge transfer, which is beneficial for the photocatalytic reduction of U(VI) in water.

Considering the "electron-sponge" property of polyoxometalates (POMs), which enables POMs to maintain structural integrity when they gain or lose electrons, POMs can effectively promote the separation and transfer of photogenerated carriers.[30–34] In this work, we designed and synthesized a perovskite nanotube array-based catalyst encapsulated by functionalized POMs as a water-proof material, $(HMTA)_3Pb_2Br_7$@STA-PW_{12}, which can maintain stability in water for 10 hours under stirring conditions. It is noteworthy that STA-PW_{12} not only increases the stability of the catalyst in water due to the hydrophobic long-chain STA but also contributes to the separation of photogenerated carriers and enhances charge transfer from $(HMTA)_3Pb_2Br_7$ to the $[PW_{12}O_{40}]^{3-}$ anionic cluster, which acts as a charge transfer medium to improve the photocatalytic performance. The enhanced electron carrier mobility (μ_e) (1.1 $cm^2\ V^{-1}\ s^{-1}$) and carrier diffusion length (245 nm) of $(HMTA)_3Pb_2Br_7$@STA-PW_{12} further illustrate its effective charge carrier transfer, which is also confirmed through transient photocurrent response measurements and density functional theory (DFT) calculations. Finally, the synthesized catalyst exhibits excellent performance in the photocatalytic removal of U(VI) with a removal rate of 99.3% at a U(VI) concentration of 40 ppm after 40 min under simulated sunlight.

Results and discussion

Structure and characterization of the $(HMTA)_3Pb_2Br_7$ nanotube array and composite $(HMTA)_3Pb_2Br_7$@STA-PW_{12}

Nanoscale $(HMTA)_3Pb_2Br_7$ MHPs were obtained by conventional solvent method according to a previous literature procedure with some modifications.[35] In brief, certain amounts of lead(II) bromide and hexamethylenetetramine hydrobromide were mixed and dissolved in DMF to form a clear precursor solution, and then a large amount of DCM acting as a poor solution was quickly added to the aforementioned solution and supersonically dispersed for 30 minutes. Nanoscale and high-quality $(HMTA)_3Pb_2Br_7$ MHPs could be harvested. The detailed synthetic process of 1D nanotube $(HMTA)_3Pb_2Br_7$ and compo-

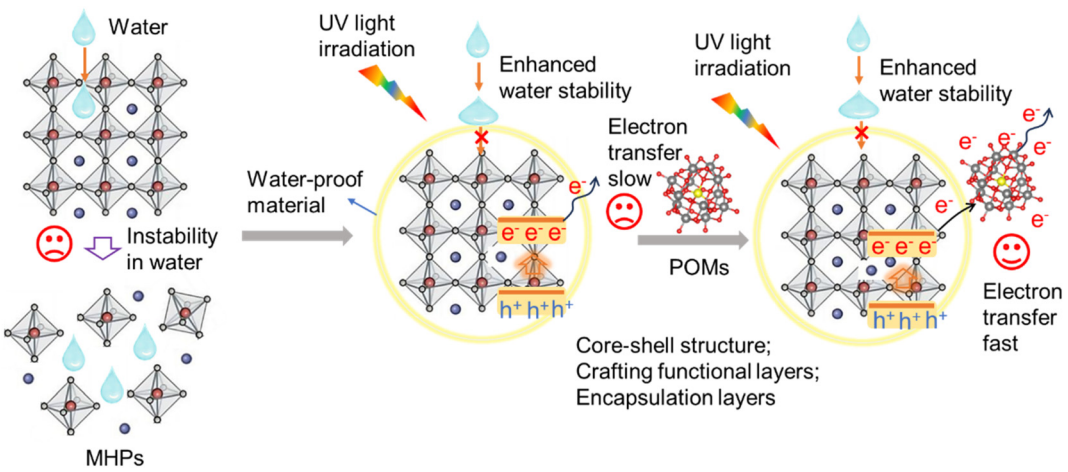

Scheme 1 Schematic of constructing MHPs with enhanced water stability and excellent carrier transfer capability.

site $(HMTA)_3Pb_2Br_7$@STA-PW_{12} material can be obtained from the Experimental section. As shown in Fig. S1,† the basic structural motif of $(HMTA)_3Pb_2Br_7$ is composed of one lead bromide dimer $[Pb_2Br_7]^{3-}$ and three protonated HMTA ($C_6H_{13}N_4^+$). The six lead bromide dimers connect at the corners to form rugged rings with an inner diameter of about 11.04 Å (Fig. S2†), which extends in one-dimensional direction (Fig. 1a). The protonated HMTA cations acting as the counter cation are anchored by hydrogen bonding and coulombic interactions. It is worth noting that $(HMTA)_3Pb_2Br_7$ is a very rare one-dimensional nanotube structure (Fig. 1c) in perovskite materials, which may have better carrier transport capability compared to traditional 1D MHPs. Furthermore, adjacent 1D single nanotube $(HMTA)_3Pb_2Br_7$ forms fascinating 1D nanotube array (Fig. 1b and d) through the supramolecular interaction of hydrogen bonding between HMTA cations and $[Pb_2Br_7]^{3-}$ anions (Fig. S3†). Considering that stearyltrimethylammonium bromide (STAB) has excellent hydrophobic property and "electron-sponge" property of $H_3PW_{12}O_{40}$ (PW_{12}), we constructed composite $(HMTA)_3Pb_2Br_7$@STA-PW_{12} materials using functional STA-PW_{12}, modifying the 1D nanotube array $(HMTA)_3Pb_2Br_7$ MHPs. As shown in Fig. 1e, covering the surface of $(HMTA)_3Pb_2Br_7$ with STA-PW_{12} through the supramolecular interactions of electrostatic and hydrogen bonding interactions may enhance its stability in water. In addition, the PW_{12} in $(HMTA)_3Pb_2Br_7$@STA-PW_{12} acting as the electronic medium may be conducive to the separation of photogenerated carriers and electron transfer.

Powder X-ray diffraction (PXRD) was performed to confirm the successful synthesis of 1D nanotube $(HMTA)_3Pb_2Br_7$ MHPs and composite $(HMTA)_3Pb_2Br_7$@STA-PW_{12} material. As shown in Fig. 2a, the PXRD pattern of the synthesized 1D nanotube $(HMTA)_3Pb_2Br_7$ MHPs matches well with its simulated one from the simulated single crystal data, illustrating its good phase purity. It should be noted that due to the amorphous characteristics of STAB and rapid crystallization process of STA-PW_{12}, only one strong peak at 8.60° can be observed, which demonstrates its imperfect crystallinity. Notably, 1D nanotube $(HMTA)_3Pb_2Br_7$ MHPs has a diffraction peak at 8.33° for the (200) crystal plane, which can be distinguished easily from STA-PW_{12}. In addition, during the synthetic process, the molar ratio of PW_{12} and $(HMTA)_3Pb_2Br_7$ plays a crucial role in the successful synthesis of $(HMTA)_3Pb_2Br_7$@STA-PW_{12}. As shown in Fig. 2a, when the molar ratio of PW_{12} and $(HMTA)_3Pb_2Br_7$ is 1/3, $(HMTA)_3Pb_2Br_7$@STA-PW_{12} can be harvested successfully. We further investigated the stability of $(HMTA)_3Pb_2Br_7$@STA-PW_{12} in water. As illustrated in Fig. 2b, the state of $(HMTA)_3Pb_2Br_7$@STA-PW_{12} can maintain stability

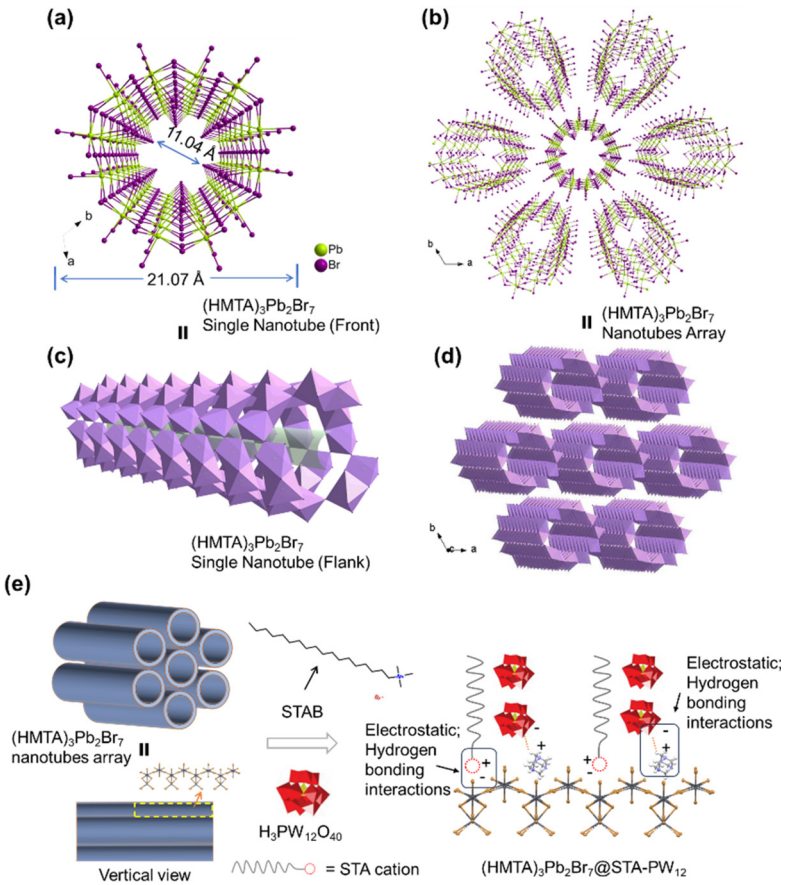

Fig. 1 1D nanotube structure of $(HMTA)_3Pb_2Br_7$ from the front (a) and flank (c) directions; nanotube array structure of $(HMTA)_3Pb_2Br_7$ from the front (b) and flank (d) directions; (e) schematic for the preparation of $(HMTA)_3Pb_2Br_7$@STA-PW_{12}.

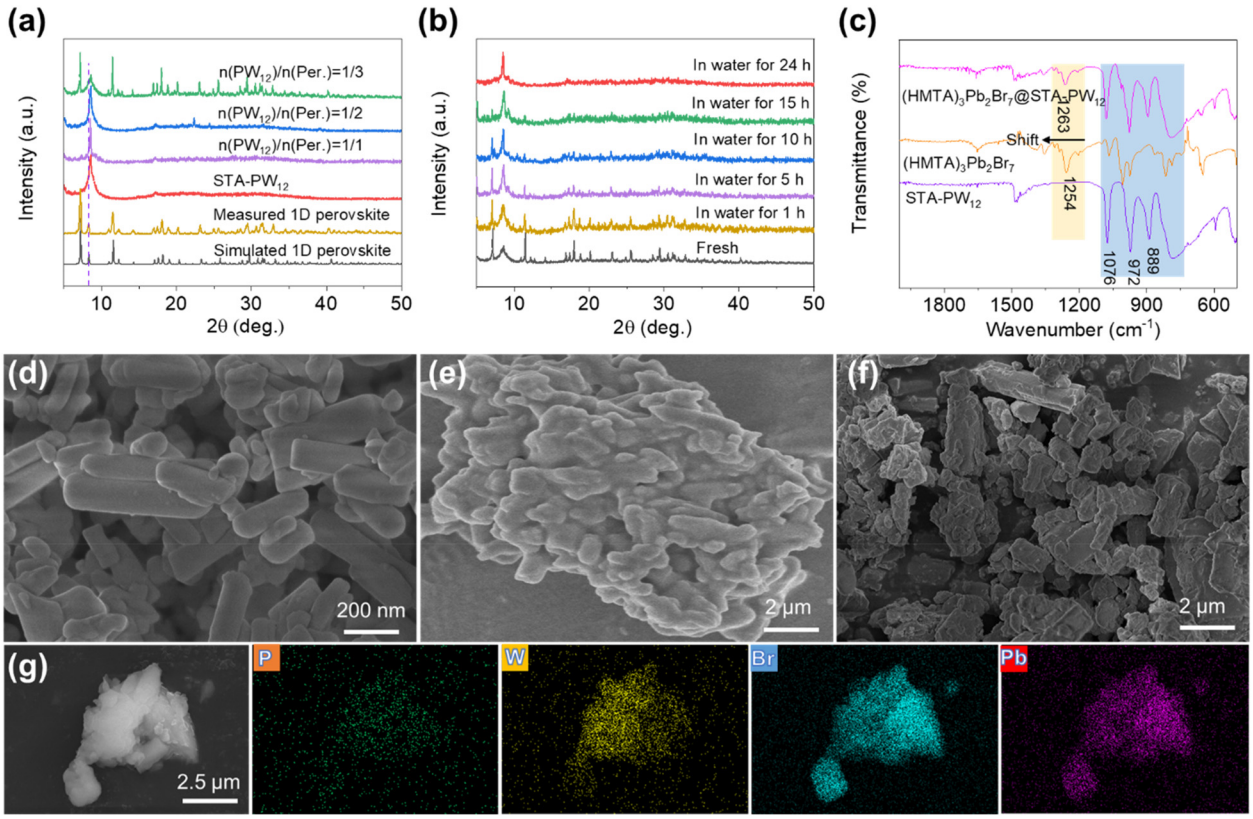

Fig. 2 (a) PXRD patterns of the synthesized $(HMTA)_3Pb_2Br_7$ and its simulated one from the single crystal data as well as patterns of $(HMTA)_3Pb_2Br_7$@STA-PW_{12} under different molar ratios of raw materials; (b) PXRD patterns of $(HMTA)_3Pb_2Br_7$@STA-PW_{12} after immersing in water; (c) FTIR spectra of STA-PW_{12}, $(HMTA)_3Pb_2Br_7$ and $(HMTA)_3Pb_2Br_7$@STA-PW_{12}, respectively; (d–f) SEM images of $(HMTA)_3Pb_2Br_7$, STA-PW_{12}, and $(HMTA)_3Pb_2Br_7$@STA-PW_{12}, respectively; (g) EDS mapping of $(HMTA)_3Pb_2Br_7$@STA-PW_{12} composites (including P, W, Br, and Pb elements).

for about 10 hours under stirring conditions, which leaves the operation window for the photocatalytic reduction of U(VI). To further confirm its stability in water, we performed Fourier transform infrared (FTIR) spectra tests on STA-PW_{12} powder, $(HMTA)_3Pb_2Br_7$ samples and $(HMTA)_3Pb_2Br_7$@STA-PW_{12} powder samples, respectively. From Fig. 2c, it can be seen that some characteristic absorption bands of $(HMTA)_3Pb_2Br_7$ can also be found in $(HMTA)_3Pb_2Br_7$@STA-PW_{12} after immersing them in water for 10 hours under stirring conditions. A strong peak located at 1254 cm^{-1} in the $(HMTA)_3Pb_2Br_7$ powder samples, which is attributed to the C–N bonds' stretching vibration of HMTA (Fig. 2c), is slightly blue-shifted to 1263 cm^{-1} after modification by STA-PW_{12}, which indicates that their supramolecular molecular interaction of hydrogen bonding. In addition, the characteristic peaks at 1076 cm^{-1}, 972 cm^{-1} and 889 cm^{-1} of PW_{12} can also be observed in the $(HMTA)_3Pb_2Br_7$@STA-PW_{12} powder samples after stirring them for 10 hours in water. These results demonstrate that $(HMTA)_3Pb_2Br_7$@STA-PW_{12} can maintain stability in water for 10 hours under stirring conditions. We further compared the durability of $(HMTA)_3Pb_2Br_7$@STA-PW_{12} in water with some other perovskites, as shown in Table S1.† The results indicate that $(HMTA)_3Pb_2Br_7$@STA-PW_{12} possesses excellent stability in water. In order to evaluate the acid–base tolerance of $(HMTA)_3Pb_2Br_7$@STA-PW_{12}, PXRD patterns were measured at various pH values (2–12). When $(HMTA)_3Pb_2Br_7$@STA-PW_{12} was immersed into aqueous solutions with different pH values for 1 h at 25 °C, no obvious peak changes were observed in the PXRD patterns (Fig. S4†), indicating that $(HMTA)_3Pb_2Br_7$@STA-PW_{12} possesses excellent acid–base tolerance. The morphologies of the 1D nanotube $(HMTA)_3Pb_2Br_7$ MHPs and $(HMTA)_3Pb_2Br_7$@STA-PW_{12} composites were investigated using SEM. It can be clearly seen that $(HMTA)_3Pb_2Br_7$ exhibits a smooth surface and sharp fringe with a size of 100–400 nm (Fig. 2d). However, as shown in Fig. 2e, STA-PW_{12} shows a rough, irregular surface and bulk morphology with a size of 0.5–3 μm, which is consistent with its imperfect crystallinity. The morphology of $(HMTA)_3Pb_2Br_7$@STA-PW_{12} composites is significantly different from that of 1D nanotube $(HMTA)_3Pb_2Br_7$ MHPs because of the wrapping of STA-PW_{12}, showing a rough and irregular surface (Fig. 2f), which is consistent with the transmission electron microscopy (TEM) images (Fig. S5†). The nanosizing of 1D nanotube $(HMTA)_3Pb_2Br_7$ MHPs is a prerequisite for it to be encapsulated by the micron level STA-PW_{12}. In addition, EDS mapping of $(HMTA)_3Pb_2Br_7$@STA-PW_{12} indicates that P, W, Br and Pb are uniformly dispersed in the composites (Fig. 2g), which is consistent with the PXRD and FTIR measurements. Fig. S6†

displays the high-resolution X-ray photoelectron spectroscopy (XPS) spectra of P 2p, W 4f, Br 3d and Pb 46 of $(HMTA)_3Pb_2Br_7$@STA-PW_{12}. As shown in Fig. S6a and S6b,† the binding energy peak at 134.1 eV can be attributed to the characteristic peak of P 2p of P^{5+}, and peaks at 37.7 and 35.6 eV are characteristic peaks of W $4f_{5/2}$ and W $4f_{7/2}$ of W^{6+}. Fig. S6c and S6d† show that Br^- and Pb^{2+} exist in single valence state, respectively. All these results demonstrate that the $(HMTA)_3Pb_2Br_7$@STA-PW_{12} composite catalyst was successfully synthesized.

Excellent optical and photoelectrochemical properties

To reveal the intrinsic semiconductor properties of $(HMTA)_3Pb_2Br_7$@STA-PW_{12}, the transient photocurrent responses was firstly explored to evaluate the separation efficiency of photogenerated carriers. As shown in Fig. 3a, the photocurrent density of $(HMTA)_3Pb_2Br_7$@STA-PW_{12} can reach as high as 15.4 μA cm^{-2}, which is 3 times more than that of $(HMTA)_3Pb_2Br_7$ (4.8 μA cm^{-2}). The higher current density illustrates the improved separation efficiency of photogenerated carriers and enhanced charges transfer capability of $(HMTA)_3Pb_2Br_7$@STA-PW_{12}. The Nyquist plots obtained from the electrochemical impedance spectra (EIS) of $(HMTA)_3Pb_2Br_7$@STA-PW_{12} and $(HMTA)_3Pb_2Br_7$ were measured

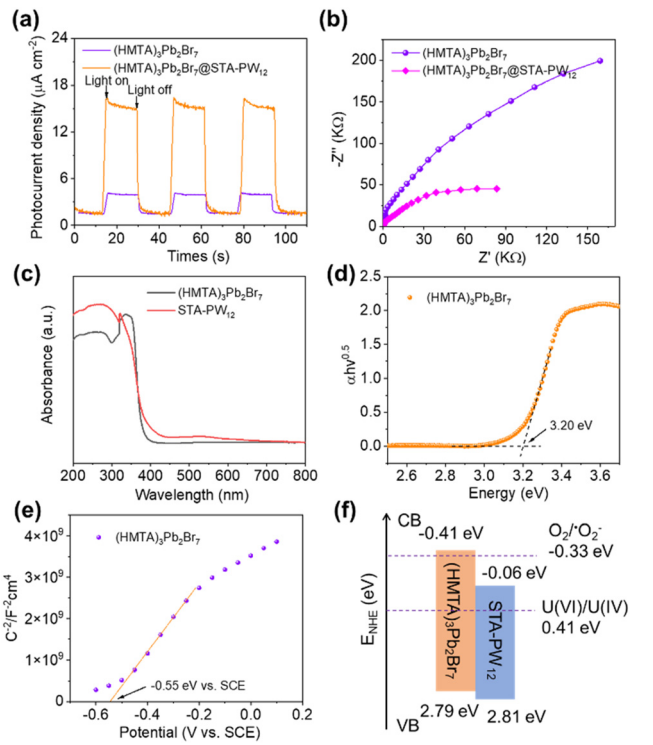

Fig. 3 (a) Transient photocurrent responses of $(HMTA)_3Pb_2Br_7$@STA-PW_{12} and $(HMTA)_3Pb_2Br_7$ under 0.5 V bias voltage; (b) EIS curves of $(HMTA)_3Pb_2Br_7$@STA-PW_{12} and $(HMTA)_3Pb_2Br_7$; (c) UV-vis diffuse reflectance spectra of STA-PW_{12} and $(HMTA)_3Pb_2Br_7$ samples; (d) Tauc plot of $(HMTA)_3Pb_2Br_7$. (e) Mott–Schottky plot of $(HMTA)_3Pb_2Br_7$; (f) electronic band structure diagram of $(HMTA)_3Pb_2Br_7$@STA-PW_{12}.

to evaluate the interfacial charge transfer (Fig. 3b). The radius of $(HMTA)_3Pb_2Br_7$@STA-PW_{12} is smaller than that of $(HMTA)_3Pb_2Br_7$, which means that the charge transfer of $(HMTA)_3Pb_2Br_7$@STA-PW_{12} is faster than that of $(HMTA)_3Pb_2Br_7$. The electronic band structures of $(HMTA)_3Pb_2Br_7$ and STA-PW_{12} were then identified to investigate the charges carriers' separation and transfer mechanism for the $(HMTA)_3Pb_2Br_7$@STA-PW_{12}. The UV-vis diffuse reflectance spectra of $(HMTA)_3Pb_2Br_7$ and STA-PW_{12} powder samples were measured to evaluate their bandgap (E_g) (Fig. 3c). E_g can be defined as the intersection point between the energy axis and the line extrapolated from the linear portion of the adsorption edge in the plot of Kubelka–Munk function F against E. $F = (1 - R)^2/2R$ was transformed from the measured diffuse reflectance data, in which R presents the reflectance of an infinitely thick layer at a given wavelength.[36] The bandgaps of $(HMTA)_3Pb_2Br_7$ and STA-PW_{12} were calculated to be 3.20 eV and 2.87 eV, respectively (Fig. 3d and Fig. S7†). Then, Mott–Schottky plots were recorded to evaluate the conduction band minimum (CBM). As shown in Fig. 3e, the flat band potential (E_{fb}) of $(HMTA)_3Pb_2Br_7$ was calculated to be −0.55 eV *vs.* SCE, corresponding to −0.31 eV *vs.* NHE. Considering that the CBM could be 0–0.1 eV more negative than the E_{fb}, the CBM of $(HMTA)_3Pb_2Br_7$ equals −0.41 eV *vs.* NHE. Also, STA-PW_{12} was calculated to be −0.06 eV *vs.* NHE (Fig. S8†). The position of the valence band maximum (VBM) of $(HMTA)_3Pb_2Br_7$ and STA-PW_{12} were 2.79 eV and 2.81 eV, respectively, based on the bandgaps and CBM. According to the results of Tauc plots and Mott–Schottky plots, the electronic band structure diagram of $(HMTA)_3Pb_2Br_7$@STA-PW_{12} was drawn (Fig. 3f). Due to the well-matched energy level structure between $(HMTA)_3Pb_2Br_7$ and STA-PW_{12}, the photogenerated carriers' separation efficiency and transfer capacity can be significantly enhanced, which is also consistent with the measurements of transient photocurrent responses.

Enhancing the carrier transport capability

To further reveal the separation efficiency of photogenerated carriers and carrier diffusion lengths of $(HMTA)_3Pb_2Br_7$ and $(HMTA)_3Pb_2Br_7$@STA-PW_{12}, respectively, the steady-state photoluminescence (PL) and time-resolved photoluminescence (TRPL) spectra were firstly measured. As shown in Fig. 4a, the relatively lower steady-state photoluminescence (PL) emission for $(HMTA)_3Pb_2Br_7$@STA-PW_{12} compared to that of $(HMTA)_3Pb_2Br_7$ is due to the recombination of photogenerated carriers being effectively suppressed, indicating the low exciton binding energy and favorable charges transport, which is consistent with the transient photocurrent measurements. To affirm this result, the time-resolved photoluminescence (TRPL) spectra of $(HMTA)_3Pb_2Br_7$@STA-PW_{12} and $(HMTA)_3Pb_2Br_7$ were further measured. Fig. 4b shows that $(HMTA)_3Pb_2Br_7$@STA-PW_{12} displays shorter lifetimes (21.2 ns) compared to $(HMTA)_3Pb_2Br_7$ (98.5 ns), which illustrates the higher separation efficiency and transfer ability of photogenerated charges of $(HMTA)_3Pb_2Br_7$@STA-PW_{12}. The BCP 8 nm and Cu 20 nm were deposited on two surfaces of

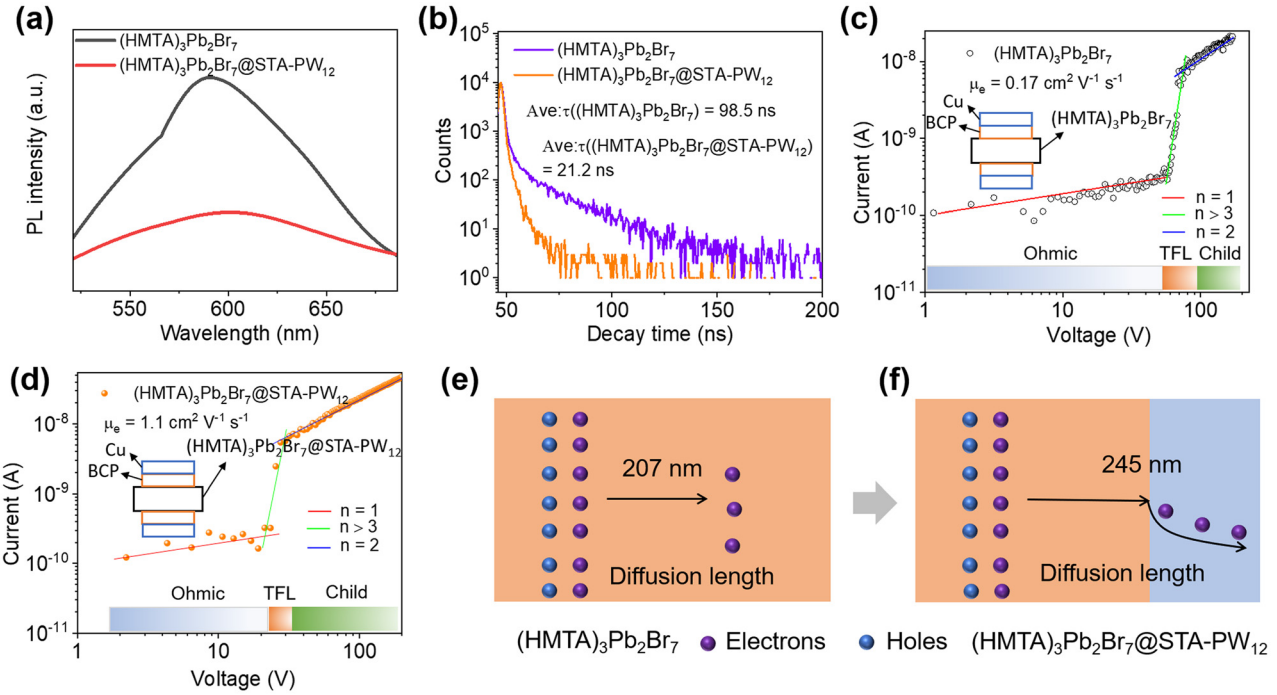

Fig. 4 (a) PL and (b) TRPL spectra of $(HMTA)_3Pb_2Br_7$@STA-PW_{12} and $(HMTA)_3Pb_2Br_7$, respectively; current–voltage curves for electron-only wafer devices of (c) $(HMTA)_3Pb_2Br_7$ and (d) $(HMTA)_3Pb_2Br_7$@STA-PW_{12}, respectively; (e) schematic of carrier diffusion length of $(HMTA)_3Pb_2Br_7$ samples; (f) schematic of carrier diffusion length of the $(HMTA)_3Pb_2Br_7$@STA-PW_{12} sample.

$(HMTA)_3Pb_2Br_7$ and $(HMTA)_3Pb_2Br_7$@STA-PW_{12} wafers, respectively, by thermal evaporation under 5×10^{-4} Pa. Then, the two electrodes of the wafers are respectively connected with thin copper wires (Fig. S9†). Carrier mobility (μ) is an important quality factor that measures the transfer ability of electrons or holes in semiconducting materials. We quantitatively harvested the electrons carrier mobility μ_e of $(HMTA)_3Pb_2Br_7$@STA-PW_{12} and $(HMTA)_3Pb_2Br_7$ wafers using a space charge-limited current (SCLC) method. As illustrated in Fig. 4c and d, the current increased from the linear ohmic region, through a trap-filled limited (TFL) region, and finally to the quadratic Child's region with increasing bias voltage. μ_e can be calculated from the Child's region using the equation[37] $J_D = \frac{9\varepsilon\varepsilon_0\mu V^2}{8L^3}$, where J_D is the current density, V represents the bias voltage, and ε_0 is the vacuum permittivity. The μ_e of the $(HMTA)_3Pb_2Br_7$@STA-PW_{12} wafer was calculated to be 1.10 $cm^2\ V^{-1}\ s^{-1}$, which is 6 times higher than that of $(HMTA)_3Pb_2Br_7$ (0.17 $cm^2\ V^{-1}\ s^{-1}$), indicating that the transport capacity of charge carriers in $(HMTA)_3Pb_2Br_7$@STA-PW_{12} is enhanced compared to that of $(HMTA)_3Pb_2Br_7$. Carrier diffusion lengths (L_D) can be evaluated from the PL lifetimes (τ) and the values of carrier mobility (μ) using the relation[38] $L_D = \sqrt{\frac{Tk_B}{e} \times \mu\tau}$, where k_B is the Boltzmann constant, T is the temperature in Kelvin, and e is the electron charge. The calculated L_D of $(HMTA)_3Pb_2Br_7$@STA-PW_{12} is 245 nm (Fig. 4f), which is obviously higher than that of $(HMTA)_3Pb_2Br_7$ (207 nm) (Fig. 4e), further indicating that photogenerated carriers are more easily separated and diffused in $(HMTA)_3Pb_2Br_7$@STA-PW_{12}.

Photocatalytic removal of U(VI)

Considering that $(HMTA)_3Pb_2Br_7$@STA-PW_{12} possesses excellent stability in water and efficient carriers' transport capability, the performance of $(HMTA)_3Pb_2Br_7$@STA-PW_{12} samples for the photocatalytic reduction of U(VI) under simulated sunlight was systematically studied. The relationship between the U(VI) removal rate and the solid–liquid ratio over the $(HMTA)_3Pb_2Br_7$@STA-PW_{12} catalyst is depicted in Fig. 5a. It is clear that the adsorption rate of $(HMTA)_3Pb_2Br_7$@STA-PW_{12} on U(VI) increases from 16.1% to 36.9% at equilibrium period in dark with the solid–liquid ratio increasing from 0.2 to 0.8 g L^{-1}, which is a prerequisite for achieving highly efficient photoreduction of U(VI). After the light is turned on, the best removal rate of U(VI) can reach as high as 99.3% at a solid–liquid ratio of 0.6 g L^{-1}, which is higher than that the removal rate at other solid–liquid ratios. Furthermore, the reaction rate constant (k) was calculated by pseudo first order kinetics equation[39] $\ln(C_t/C_0) = -k_t$, where C_t and C_0 represent the residual U(VI) and initial U(VI) concentrations at time t after the photocatalytic process, respectively. From Fig. S10,† it can be seen that the k value at a solid–liquid ratio of 0.6 g L^{-1} (0.114 min^{-1}) is obviously larger than that at 0.2 g L^{-1} (0.008 min^{-1}), 0.4 g L^{-1} (0.019 min^{-1}) and 0.8 g L^{-1} (0.066 min^{-1}), which further indicates that using

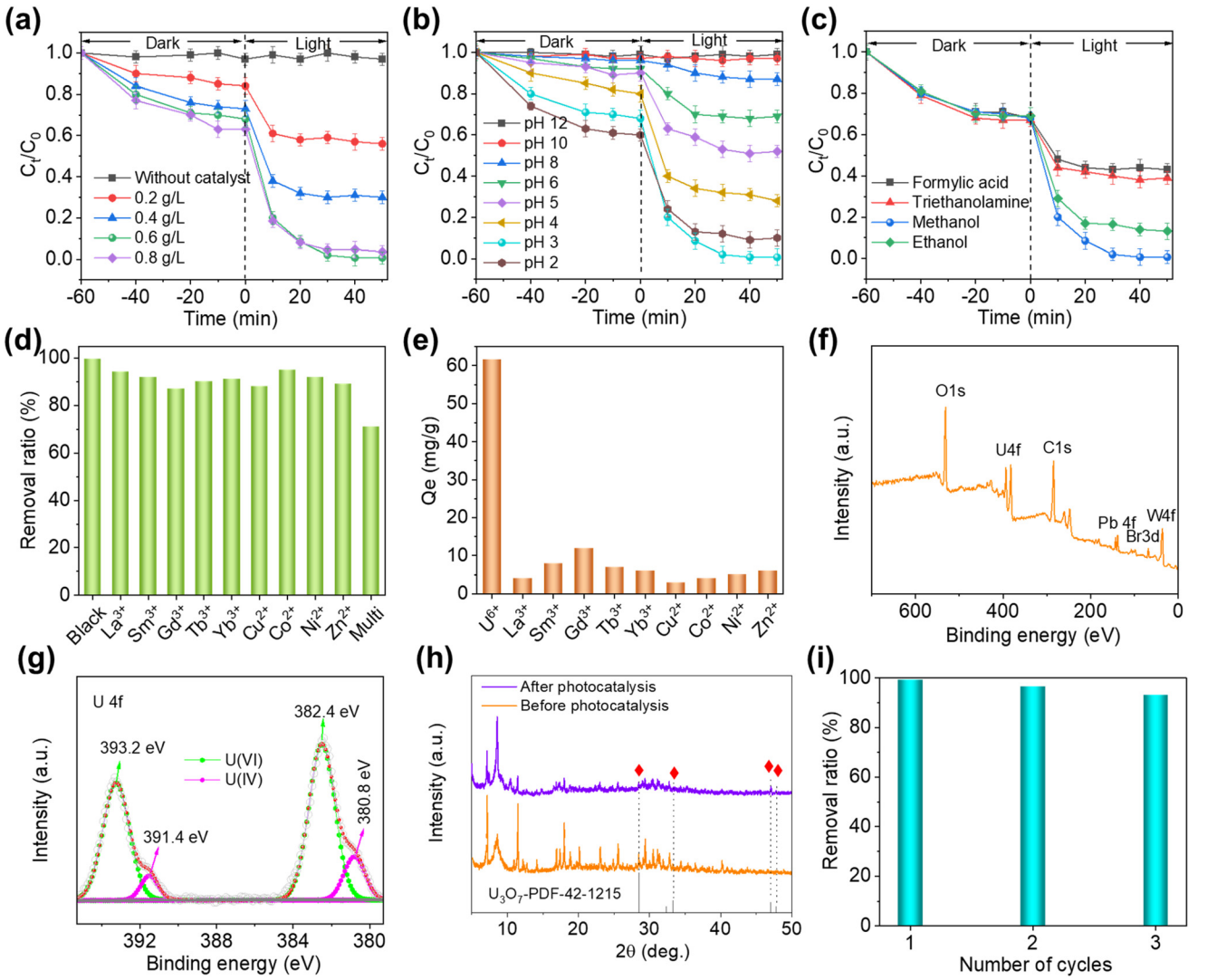

Fig. 5 Influence of solid–liquid ratio (a) on catalytic performance, (b) pH values of solution, (c) different hole sacrificial reagents on photocatalytic performance; (d) effect of $(HMTA)_3Pb_2Br_7$@STA-PW_{12} on the U(VI) removal rate under different competitive metal ions and multiple competing ions; (e) adsorption capacity of $(HMTA)_3Pb_2Br_7$@STA-PW_{12} for different metal ions. (f) XPS spectrum of $(HMTA)_3Pb_2Br_7$@STA-PW_{12} after photocatalysis; (g) high-resolution XPS spectrum of U 4f after photocatalysis; (h) PXRD patterns of $(HMTA)_3Pb_2Br_7$@STA-PW_{12} before and after photocatalysis; (i) photocatalytic cycling experiment for U(VI) reduction.

$(HMTA)_3Pb_2Br_7$@STA-PW_{12} as a catalyst for the photoreduction of U(VI), the ideal solid–liquid ratio is 0.6 g L^{-1}. Generally, the pH of a solution is always a key factor for the photocatalytic reduction of metal ions due to its close correlation with the surface charge of catalysts. Thus, the effect of pH of the solution on the photocatalytic reduction of U(VI) was evaluated by changing the pH values from 2 to 12. Zeta potential curve (Fig. S11†) indicates that the surface of the $(HMTA)_3Pb_2Br_7$@STA-PW_{12} catalyst possesses negative charges in the pH range from 2 to 6 and positive charges in the pH range of 8 to 12. As shown in Fig. 5b, with a decrease in the pH value, the adsorption ability for U(VI) over $(HMTA)_3Pb_2Br_7$@STA-PW_{12} gradually increases, which is mainly because the electrostatic attraction between $(HMTA)_3Pb_2Br_7$@STA-PW_{12} and U(VI) is gradually strengthening as the surface charges of $(HMTA)_3Pb_2Br_7$@STA-PW_{12} gradually become more negative, which is consistent with the zeta potentials. At pH 3, U(VI) can be almost completely removed with a removal rate of 99.3%, which is larger than that of other pH values. Notably, $(HMTA)_3Pb_2Br_7$@STA-PW_{12} exhibits negligible catalytic activity for U(VI) extraction due to the electrostatic repulsion between $(HMTA)_3Pb_2Br_7$@STA-PW_{12} and U(VI). Moreover, the k value at pH 3 (0.114 min^{-1}) is also larger than that at other pH values (Fig. S12†). Notably, although $(HMTA)_3Pb_2Br_7$@STA-PW_{12} possesses stronger adsorption capacity at pH 2, the removal rate and the reaction rate constant (k = 0.045 min^{-1} at pH 2) are lower than that at pH 3. Thus, pH 3 was selected as the optimal pH. Hole sacrificial reagents in a photocatalytic system can consume holes, which prevents the recombination of photogenerated electron–hole

pairs on the semiconductor surface, thus enhancing the photocatalytic efficiency. Fig. 5c shows the effect of different hole sacrificial reagents including methanol, ethanol, triethanolamine and formic acid on the photocatalytic performance. Under the same conditions, methanol and ethanol prove to be more effective hole sacrificial reagents than formic acid and triethanolamine, which is probably because the –COOH or $–NH_2$ groups of formic acid and triethanolamine may coordinate with U(VI) ions, which hinders U(VI) adsorption on the catalyst and obstructs the photocatalytic progress. In addition, the photocatalytic performance using methanol as the hole sacrificial reagent is higher than that of ethanol. Thus, methanol was selected as the hole sacrificial reagent for the photocatalytic reduction of U(VI) in this system.

Considering that the actual radioactive wastewater contains different metal ions, which may compete with U(VI) in the process of adsorption or photocatalysis, equivalent different amounts of competitive ions were added to investigate the adsorption and photocatalytic performance of the catalyst. As shown in Fig. 5d, the solution containing La^{3+}, Sm^{3+}, Gd^{3+}, Tb^{3+}, Yb^{3+}, Co^{2+}, Co^{2+}, Ni^{2+}, Zn^{2+} and multiple competing ions was selected to explore the effect of different competitive ions on the performance of photocatalytic removal of U(VI). The results show that these competing ions in this photocatalytic system have negligible effect on the removal rate of U(VI), while the removal rate in a solution containing multiple competing ions displays a slight decrease, which may be due to the combined effect of different competitive metal ions. Considering that the good adsorption capacity for reaction substrates is a prerequisite for the photocatalytic process, we further investigated the discrepancies in the adsorption capacity for different competitive metal ions using $(HMTA)_3Pb_2Br_7$@STA-PW_{12} catalyst. As shown in Fig. 5e, the Q_e of U(VI) at equilibrium period in dark can reach as high as 61 mg g^{-1}, which is significantly higher than that of competitive metal ions, further indicating that these competitive metal ions have negligible effect on the removal rate of U(VI). To demonstrate the successful photocatalytic reduction of U(VI) to U(IV), XPS and PXRD measurements were carried out to investigate the $(HMTA)_3Pb_2Br_7$@STA-PW_{12} catalyst after the photocatalytic process. The full spectrum scanning of $(HMTA)_3Pb_2Br_7$@STA-PW_{12} samples after photocatalysis is shown in Fig. 5f. It can be clearly seen that there are spectral lines of W, Pb, Br and U elements in the spectrum of $(HMTA)_3Pb_2Br_7$@STA-PW_{12}, which illustrates that U exists on the surface of the catalyst. Fig. 5g displays the high-resolution spectrum of U 4f, and the binding energy peaks at 393.2 eV and 382.4 eV are characteristic peaks of U^{6+}, while the peaks at 391.4 eV and 380.8 eV can be attributed to U^{4+},[40] which demonstrates that U(VI) was successfully reduced in the reaction. As shown in Fig. 5h, some new peaks for the PXRD pattern of $(HMTA)_3Pb_2Br_7$@STA-PW_{12} after photocatalysis at 28.1°, 32.4°, 47°, 47.8° were observed, which can be attributed to the diffraction peaks of U_3O_7 (PDF# 42-1215) (Fig. 5h and Fig. S13†). This indicates that U(VI) was successfully reduced to products with a structure similar to U_3O_7, which is consistent with the XPS results. Reusability and stability are important figure-of-merits to evaluate a catalyst. As shown in Fig. 5i, only a slight decrease in the efficiency for the photocatalytic removal of U(VI) (from 99.3% to 93.1%) was found after three cycling experiments, indicating that the structural framework of $(HMTA)_3Pb_2Br_7$@STA-PW_{12} is basically stable after three cycles.

Photocatalytic mechanism analysis

To reveal the charge transfer process and mechanism of photocatalytic reduction of U(VI) using $(HMTA)_3Pb_2Br_7$@STA-PW_{12} catalyst, DFT calculations are conducted. As illustrated in Fig. 6a, the electron density of the HOMO orbital of $(HMTA)_3Pb_2Br_7$@STA-PW_{12} is mostly concentrated on the Br 4p and Pb 6s orbitals of 1D $(HMTA)_3Pb_2Br_7$. The LUMO orbitals of $(HMTA)_3Pb_2Br_7$@STA-PW_{12} mainly lie on the W 5d and O 2p orbitals of the $\{PW_{12}\}$ cluster. Calculated results show that the electrons of the STA-PW_{12} chains-functionalized 1D $(HMTA)_3Pb_2Br_7$ primarily transition from the Br 4p and Pb 6s orbitals of the 1D $(HMTA)_3Pb_2Br_7$ to the W 5d and O 2p orbi-

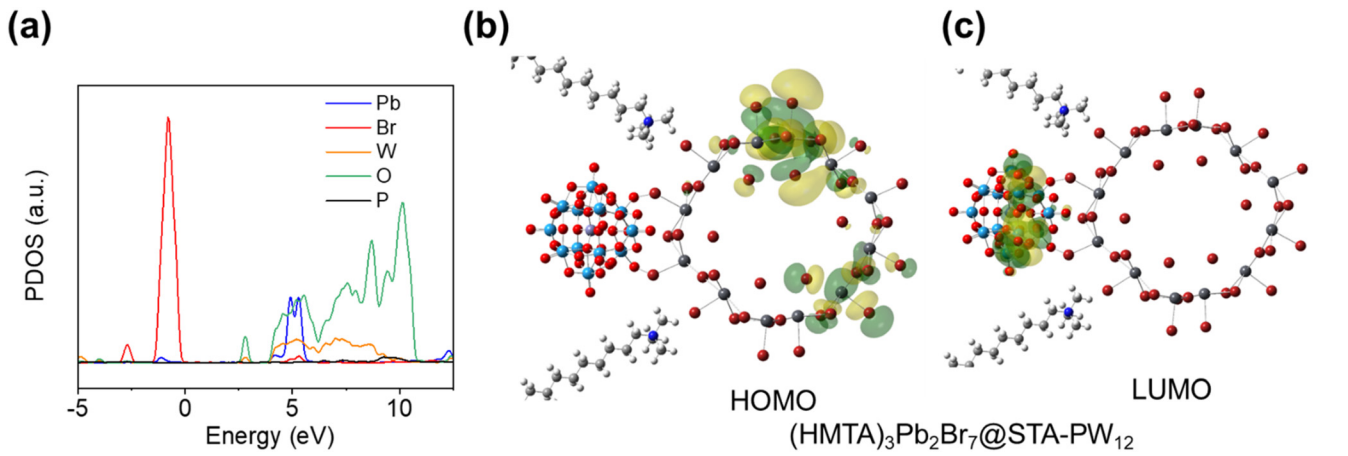

Fig. 6 (a) PDOS plots of $(HMTA)_3Pb_2Br_7$@STA-PW_{12}; (b) HOMO and (c) LUMO of $(HMTA)_3Pb_2Br_7$@STA-PW_{12}.

tals of the {PW_{12}} clusters (Fig. 6b and c), indicating the efficient separation of photogenerated carriers. Furthermore, we investigated potential adsorption models for UO_2^{2+} on $(HMTA)_3Pb_2Br_7$@STA-PW_{12} and calculated the adsorption energy (E_{ad}). The bridging oxygen atom (O_b) of PW_{12} exhibits stronger adsorption capacity for UO_2^{2+} than the terminal oxygen atom (O_t), with adsorption energy of 0.26 eV (Fig. S14†). In addition, the adsorption capacity of O_t for UO_2^{2+} at different positions is basically the same (0.16 eV for E_{ad}(i); 0.17 eV for E_{ad}(ii)). These results indicate that O_t and O_b of (PW_{12}) can all serve as binding sites for uranyl ions. It is noteworthy that the CMB of STA-PW_{12} is more negative than the redox potential of UO_2^{2+}/UO_2 (0.411 V *vs.* NHE); thus,[41] theoretically, $(HMTA)_3Pb_2Br_7$@STA-PW_{12} can photocatalytically reduce U(VI). Generally, because the redox potential of $O_2/{}^{\bullet}O_2^{2-}$ (−0.33 eV *vs.* NHE)[42] is less negative than the CBM of $(HMTA)_3Pb_2Br_7$@STA-PW_{12} (−0.41 eV *vs.* NHE), O_2 may capture photogenerated electrons to produce the superoxide radical (${}^{\bullet}O_2^{2-}$) in the reaction, which reduces the utilization rate of electrons, thus not being conducive to the photocatalytic reduction of U(VI). However, as shown in Fig. S15,† the removal rates of U(VI) with O_2 and N_2 atmosphere in this system are basically the same, which may be due to the effective and fast transfer of photogenerated electrons from the CBM of $(HMTA)_3Pb_2Br_7$ to the CBM of STA-PW_{12}. The CBM of STA-PW_{12} (−0.06 eV *vs.* NHE) is negative compared to the redox potential of $O_2/{}^{\bullet}O_2^{2-}$ while positive compared to the redox potential of UO_2^{2+}/UO_2, which is consistent with the result that there is negligible effect of O_2 on the photocatalytic performance.

Based on experimental and DFT calculation results, we propose a plausible mechanism for the photocatalytic reduction of U(VI) using $(HMTA)_3Pb_2Br_7$@STA-PW_{12} catalyst (Fig. 7). First, due to the hydrophobic long-chain STA in the catalyst and effective encapsulation of $(HMTA)_3Pb_2Br_7$ by STA-PW_{12}, the $(HMTA)_3Pb_2Br_7$@STA-PW_{12} catalyst exhibits enhanced stability in water for 10 hours, which is the operation window for the photocatalytic reduction of U(VI). When the reaction system was irradiated by simulated sunlight, the photogenerated electrons transition occurs from the VBM to the CBM, leaving holes in the VBM. Considering the "electron-sponge" properties of POM, which can store and transfer electrons effectively, the photogenerated electrons in the CBM of $(HMTA)_3Pb_2Br_7$ transfer quickly to the CBM of STA-PW_{12} (O_b and O_t) due to the well-matched energy level structure. Then, methanol as a hole sacrificial agent quenched the photogenerated holes. The accumulated electrons in the O_b and O_t of STA-PW_{12} can effectively transfer to the U(VI), achieving complete U(VI)-to-U(IV) photocatalytic reduction.

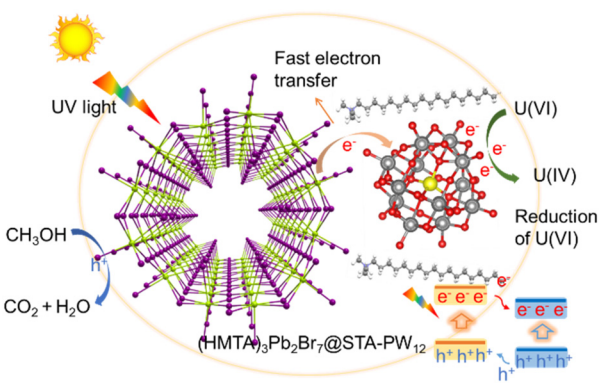

Fig. 7 Possible mechanism for the photocatalytic reduction of U(VI) using $(HMTA)_3Pb_2Br_7$@STA-PW_{12} catalyst.

Conclusions

In summary, a novel perovskite nanotube array-based catalyst encapsulated by a functionalized polyoxometalate $(HMTA)_3Pb_2Br_7$@STA-PW_{12} was constructed for the photocatalytic reduction of U(VI). Impressively, STA-PW_{12} acting as the charge transfer medium not only increases the stability of the catalyst in water due to the hydrophobic long-chain STA but also contributes to the separation of photogenerated carriers and enhances the charge transfer from $(HMTA)_3Pb_2Br_7$ to PW_{12}, which significantly improves the photocatalytic activities. The removal rate of U(VI) can reach as high as 99.3% at a U(VI) concentration of 40 ppm after 40 minutes under simulated sunlight irradiation using $(HMTA)_3Pb_2Br_7$@STA-PW_{12} catalyst. Given the intrinsic advantages of MHPs including designable architectures and chemical compositions as well as excellent optoelectronic properties, combined with the "electron-sponge" property of POMs, more versatile candidates based on perovskite catalysts modified by POMs for photocatalytic applications are visible in the future.

Experimental

Materials and characterization

All reagents utilized in this study were analytically purity and used without additional processing. Additional information regarding the reagents and instrumental characterization can be found in the ESI.†

Synthesis of 1D nanotube $(HMTA)_3Pb_2Br_7$ and composite $(HMTA)_3Pb_2Br_7$@STA-PW_{12}

For the synthesis of nanosized $(HMTA)_3Pb_2Br_7$, a mixture of lead(II) bromide ($PbBr_2$) (2.72 mmol, 1.0 g) and hexamethylenetetramine hydrobromide (HMTA) (4.09 mmol, 0.9 g) was dissolved in 30 mL of DMF and stirred for 30 minutes to form a clear precursor solution. Then, a large amount of DCM solvent (200 mL) was added to the above solution quickly and supersonically dispersed for 30 minutes. The nanosized $(HMTA)_3Pb_2Br_7$ was collected by filtration, cleaned alternately with anhydrous ethanol three times, and then dried under vacuum at 50 °C. For the synthesis of $(HMTA)_3Pb_2Br_7$@STA-PW_{12}, firstly, the synthesized nanosized $(HMTA)_3Pb_2Br_7$ (0.3 mmol, 0. 42 g) was dispersed in a 20 mL

ethanol solution with stearyltrimethylammonium bromide (STAB, 0.9 mmol, 0.35 g) dissolved in it. Then, 20 mL ethanol solution containing 0.9 mmol of $H_3PW_{12}O_{40}$ (2.6 g) was added to the above solution slowly with stirring for 1 hour. The obtained $(HMTA)_3Pb_2Br_7$@STA-PW_{12} was collected by filtration and then dried under vacuum at 50 °C.

Photocatalytic reduction experiments of uranium(VI)

The photocatalytic experiments were conducted in a quartz beaker photoreactor with a water-cooling system under simulated sunlight (300 W xenon lamp, AM 1.5 G, 100 mW cm^{-2}), and the reaction temperature was maintained at room temperature (25 ± 0.2 °C). Typically, 30 mg catalyst was added to 50 mL of 40 ppm U(VI) aqueous solutions with 0.5 M CH_3OH as the sacrificial reagent under continuous stirring. The pH of the solution was tuned by 0.1 M HNO_3 or NaOH. The suspension solution was stirred for 1 h in the dark to reach a balance of adsorption–desorption. Then, photocatalytic reduction of U(VI) under simulated sunlight irradiation was determined. To analyze the uranium concentration, 1 mL of the reaction solution was sucked out using a syringe every 30 min and filtered with 0.44 μm polyether sulfone (PES) filters. After the reaction, the concentration of residual U(VI) was determined by an inductively coupled plasma-mass spectrometer (ICP-MS).[43] Then, the removal rate (R) of U(VI) was determined as follows: $R = [(C_0 - C_t)/C_0] \times 100\%$, where C_0 represents the initial concentration of U(VI) and C_t is the concentration of U(VI) at time t. The adsorption capacity for U(VI) and competitive metal ions at adsorption equilibrium time (Q_e, mg g^{-1}) was calculated using the equation $Q_e = (C_0 - C_e)/m \times V$, where V represents the volume of the treated solution (L), m is the amount of used adsorbent (g), C_0 is the initial concentration of metal ions, and C_e is the concentration of metal ions at adsorption equilibrium time.

Data availability

The data supporting the findings of this study are available from the corresponding authors upon reasonable request.

Conflicts of interest

There are no conflicts to declare.

Acknowledgements

This work is financially supported by the National Natural Science Foundation of China (No. 22071019 and 22172022).

References

1 X.-H. Jiang, Q.-J. Xing, X.-B. Luo, F. Li, J.-P. Zou, S.-S. Liu, X. Li and X.-K. Wang, Simultaneous photoreduction of Uranium (VI) and photooxidation of Arsenic(III) in aqueous solution over g-C_3N_4/TiO_2 heterostructured catalysts under simulated sunlight irradiation, *Appl. Catal., B*, 2018, **228**, 29–38.

2 T. Feng, Y. Yuan, S. Zhao, L. Feng, B. Yan, M. Cao, J. Zhang, W. Sun, K. Lin and N. Wang, Ultrasensitive Detection of Aqueous Uranyl Based on Uranyl–Triggered Protein Photocleavage, *Angew. Chem., Int. Ed.*, 2022, **61**, e202115886.

3 W. Zhang, B. Wang, H. Cui, Q. Wan, B. Yi and H. Yang, Unveiling the exciton dissociation dynamics steered by built-in electric fields in conjugated microporous polymers for photoreduction of uranium(VI) from seawater, *J. Colloid Interface Sci.*, 2024, **662**, 377–390.

4 Y. Xie, C. Chen, X. Ren, X. Tan, G. Song and D. Chen, Coupling g-C_3N_4 nanosheets with metal-organic frameworks as 2D/3D composite for the synergetic removal of uranyl ions from aqueous solution, *J. Colloid Interface Sci.*, 2019, **550**, 117–127.

5 Y. Xie, Z. Liu, Y. Geng, H. Li, N. Wang, Y. Song, X. Wang, J. Chen, J. Wang, S. Ma and G. Ye, Uranium extraction from seawater: material design, emerging technologies and marine engineering, *Chem. Soc. Rev.*, 2023, **52**, 97–162.

6 I. G. Alhindawy, H. I. Mira, A. O. Youssef, S. M. Abdelwahab, A. A. Zaher, W. A. El-Said, E. A. Elshehy and A. M. Abdelkader, Cobalt doped titania-carbon nanosheets with induced oxygen vacancies for photocatalytic degradation of uranium complexes in radioactive wastes, *Nanoscale Adv.*, 2022, **4**, 5330–5342.

7 X. Liu, R.-X. Bi, Z.-H. Peng, L. Lei, C.-R. Zhang, Q.-X. Luo, R.-P. Liang and J.-D. Qiu, Synergistic effect of double Schottky potential well and oxygen vacancy for enhanced plasmonic photocatalytic U(VI) reduction, *J. Hazard. Mater.*, 2023, **455**, 131581.

8 N. Liu, R. Li, J. Zhu, Q. Liu, R. Chen, J. Yu, Y. Li, H. Zhang and J. Wang, Z-scheme heterojunction ZnS/WO_3 composite: Photocatalytic reduction of uranium and band gap regulation mechanism, *J. Colloid Interface Sci.*, 2023, **630**, 727–737.

9 F. Zhang, H. Dong, Y. Li, D. Fu, L. Yang, Y. Shang, Q. Li, Y. Shao, W. Gang, T. Ding, T. Chen and W. Zhu, In Situ Metal–Oxygen–Hydrogen Modified B–Tio_2@Co_2P–X S–Scheme Heterojunction Effectively Enhanced Charge Separation for Photo–assisted Uranium Reduction, *Adv. Sci.*, 2023, **11**, 2305439.

10 P. Wu, X. Yin, Y. Zhao, F. Li, Y. Yang, N. Liu, J. Liao and T. Lan, Porphyrin-based hydrogen-bonded organic framework for visible light driven photocatalytic removal of U(VI) from real low-level radioactive wastewater, *J. Hazard. Mater.*, 2023, **459**, 132179.

11 R.-X. Bi, Z.-H. Peng, L. Lei, X.-X. Wang, X. Liu, L. Zhang, R.-P. Liang and J.-D. Qiu, Enhanced photocatalytic U(VI) reduction via double internal electric field in $CoWO_4$/covalent organic frameworks p-n heterojunction, *J. Hazard. Mater.*, 2024, **475**, 134869.

12 Y. Tian, L. Xu, S. Ning, C. Wang, Y. Wang, H. Jiang, D. Yuan, F. Yu and Y. Liu, $Ti_3C_2T_x$/$Cd_{0.8}Zn_{0.2S}$ composites

constructed of Schottky heterojunction for efficient photocatalytic reduction of U(VI), *J. Colloid Interface Sci.*, 2025, **677**, 470–480.

13 Y. J. Cai, Q. X. Luo, Q. Q. Jiang, X. Liu, X. J. Chen, J. L. Liu, X. L. Mao, J. X. Qi, R. P. Liang and J. D. Qiu, Hydrogen–Bonded Cocrystals Encapsulating $CsPbBr_3$ Perovskite Nanocrystals with Enhancement of Charge Transport for Photocatalytic Reduction of Uranium, *Small*, 2024, **20**, 2310672.

14 E. Hu, Q. Chen, Q. Gao, X. Fan, X. Luo, Y. Wei, G. Wu, H. Deng, S. Xu, P. Wang, L. Liu, R. He, X. Chen, W. Zhu and Y. Zhu, Cyano–Functionalized Graphitic Carbon Nitride with Adsorption and Photoreduction Isosite Achieving Efficient Uranium Extraction from Seawater, *Adv. Funct. Mater.*, 2024, **34**, 2312215.

15 J. Lei, H. Liu, C. Yuan, Q. Chen, J.-A. Liu, F. Wen, X. Jiang, W. Deng, X. Cui, T. Duan, W. Zhu and R. He, Enhanced photoreduction of U(VI) on WO_3 nanosheets by oxygen defect engineering, *Chem. Eng. J.*, 2021, **416**, 129164.

16 H. Zhang, W. Liu, A. Li, D. Zhang, X. Li, F. Zhai, L. Chen, L. Chen, Y. Wang and S. Wang, Three Mechanisms in One Material: Uranium Capture by a Polyoxometalate–Organic Framework through Combined Complexation, Chemical Reduction, and Photocatalytic Reduction, *Angew. Chem., Int. Ed.*, 2019, **58**, 16110–16114.

17 S. Yu, C. Li, Y. Lin, J. Zhang, Y. Liu and F. Yu, Interfacial N-Ti bond modulated COFs-TiO_2 type-II heterojunctions with directional charge transfer for efficient photocatalytic uranium reduction, *Sep. Purif. Technol.*, 2024, **341**, 126888.

18 C. Ji, T. Zhu, Y. Fan, Z. Li, X. Liu, L. Li, Z. Sun and J. Luo, Localized Lattice Expansion of $FAPbBr_3$ to Design a 3D Hybrid Perovskite for Sensitive Near–Infrared Photodetection, *Angew. Chem., Int. Ed.*, 2022, **61**, e202213294.

19 Y. Gao, E. Shi, S. Deng, S. B. Shiring, J. M. Snaider, C. Liang, B. Yuan, R. Song, S. M. Janke, A. Liebman-Peláez, P. Yoo, M. Zeller, B. W. Boudouris, P. Liao, C. Zhu, V. Blum, Y. Yu, B. M. Savoie, L. Huang and L. Dou, *Nat. Chem.*, 2019, **11**, 1151–1157.

20 J. Peng, C. Q. Xia, Y. Xu, R. Li, L. Cui, J. K. Clegg, L. M. Herz, M. B. Johnston and Q. Lin, Crystallization of $CsPbBr_3$ single crystals in water for X-ray detection, *Nat. Commun.*, 2021, **12**, 1531.

21 R. Zhuang, X. Wang, W. Ma, Y. Wu, X. Chen, L. Tang, H. Zhu, J. Liu, L. Wu, W. Zhou, X. Liu and Y. Yang, Highly sensitive X-ray detector made of layered perovskite-like $(NH_4)_3Bi_2I_9$ single crystal with anisotropic response, *Nat. Photonics*, 2019, **13**, 602–608.

22 S. Park, W. J. Chang, C. W. Lee, S. Park, H.-Y. Ahn and K. T. Nam, Photocatalytic hydrogen generation from hydriodic acid using methylammonium lead iodide in dynamic equilibrium with aqueous solution, *Nat. Energy*, 2016, **2**, 16185.

23 J. S. Zhao, Y. F. Mu, L. Y. Wu, Z. M. Luo, L. Velasco, M. Sauvan, D. Moonshiram, J. W. Wang, M. Zhang and T. B. Lu, Directed Electron Delivery from a Pb–Free Halide Perovskite to a Co(II) Molecular Catalyst Boosts CO_2 Photoreduction Coupled with Water Oxidation, *Angew. Chem., Int. Ed.*, 2024, **63**, e202401344.

24 Y. Li, C. Zhuang, S. Qiu, J. Gao, Q. Zhou, Z. Sun, Z. Kang and X. Han, Cs-Cu-Cl perovskite quantum dots for photocatalytic H_2 evolution with super-high stability, *Appl. Catal., B*, 2023, **337**, 122881.

25 H. Li, J. Yu, Y. Gong, N. Lin, Q. Yang, X. Zhang and Y. Wang, Perovskite catalysts with different dimensionalities for environmental and energy applications: A review, *Sep. Purif. Technol.*, 2023, **307**, 122716.

26 Z.-C. Kong, J.-F. Liao, Y.-J. Dong, Y.-F. Xu, H.-Y. Chen, D.-B. Kuang and C.-Y. Su, Core@Shell $CsPbBr_3$@Zeolitic Imidazolate Framework Nanocomposite for Efficient Photocatalytic CO_2 Reduction, *ACS Energy Lett.*, 2018, **3**, 2656–2662.

27 S. Wan, M. Ou, Q. Zhong and X. Wang, Perovskite-type $CsPbBr_3$ quantum dots/UiO-66(NH_2) nanojunction as efficient visible-light-driven photocatalyst for CO_2 reduction, *Chem. Eng. J.*, 2019, **358**, 1287–1295.

28 K. Su, G.-X. Dong, W. Zhang, Z.-L. Liu, M. Zhang and T.-B. Lu, In Situ Coating $CsPbBr_3$ Nanocrystals with Graphdiyne to Boost the Activity and Stability of Photocatalytic CO_2 Reduction, *ACS Appl. Mater. Interfaces*, 2020, **12**, 50464–50471.

29 L. Y. Wu, Y. F. Mu, X. X. Guo, W. Zhang, Z. M. Zhang, M. Zhang and T. B. Lu, Encapsulating Perovskite Quantum Dots in Iron–Based Metal–Organic Frameworks (MOFs) for Efficient Photocatalytic CO_2 Reduction, *Angew. Chem., Int. Ed.*, 2019, **58**, 9491–9495.

30 H.-N. Wang, M. Zhang, A. M. Zhang, F.-C. Shen, X.-K. Wang, S.-N. Sun, Y.-J. Chen and Y.-Q. Lan, Polyoxometalate-Based Metal–Organic Frameworks with Conductive Polypyrrole for Supercapacitors, *ACS Appl. Mater. Interfaces*, 2018, **10**, 32265–32270.

31 J. Du, Y. Y. Ma, W. J. Cui, S. M. Zhang, Z. G. Han, R. H. Li, X. Q. Han, W. Guan, Y. H. Wang, Y. Q. Li, Y. Liu, F. Y. Yu, K. Q. Wei, H. Q. Tan, Z. H. Kang and Y. G. Li, Unraveling photocatalytic electron transfer mechanism in polyoxometalate-encapsulated metal-organic frameworks for high-efficient CO_2 reduction reaction, *Appl. Catal., B*, 2022, **318**, 121812.

32 X. X. Li, L. Zhang, J. Liu, L. Yuan, T. Wang, J. Y. Wang, L. Z. Dong, K. Huang and Y. Q. Lan, Design of Crystalline Reduction–Oxidation Cluster-Based Catalysts for Artificial Photosynthesis, *JACS Au*, 2021, **1**, 1288–1295.

33 P.-K. Wang, W.-F. Wang, K.-B. Jiang, B.-Y. Li, S.-H. Wang, F.-K. Zheng and G.-C. Guo, Efficient X-ray Detection of Polyoxometalates@Metal–Organic Frameworks Based on Host–Guest Electron Transfer, *ACS Mater. Lett.*, 2024, **6**, 1086–1093.

34 X.-L. Wang, Y. Tian, Z.-H. Chang and H. Lin, A Series of Polyoxometalate-Based Metal–Bis(pyridyl-tetrazole) Complexes with High Electrocatalytic Activity for Hydrogen Evolution Reaction in Alkaline and Acid Media, *ACS Sustainable Chem. Eng.*, 2020, **8**, 15696–15702.

35 H. Lin, C. Zhou, Y. Tian, T. Besara, J. Neu, T. Siegrist, Y. Zhou, J. Bullock, K. S. Schanze, W. Ming, M.-H. Du and

B. Ma, Bulk assembly of organic metal halide nanotubes, *Chem. Sci.*, 2017, **8**, 8400–8404.

36 K.-K. Guo, Y.-L. Yang, S.-M. Dong, F.-Y. Li, X.-Y. Jiang and L. Xu, Reassembly Synthesis of a Silverton-Type Polyoxometalate 3D Framework: Semiconducting Properties and Photocatalytic Applications, *Inorg. Chem.*, 2022, **61**, 6411–6420.

37 Y. Liu, Y. Zhang, X. Zhu, J. Feng, I. Spanopoulos, W. Ke, Y. He, X. Ren, Z. Yang, F. Xiao, K. Zhao, M. Kanatzidis and S. Liu, Triple–Cation and Mixed–Halide Perovskite Single Crystal for High–Performance X–ray Imaging, *Adv. Mater.*, 2021, **33**, 2006010.

38 E. Alarousu, A. M. El-Zohry, J. Yin, A. A. Zhumekenov, C. Yang, E. Alhabshi, I. Gereige, A. AlSaggaf, A. V. Malko, O. M. Bakr and O. F. Mohammed, Ultralong radiative states in hybrid perovskite crystals: compositions for submillimeter diffusion lengths, *J. Phys. Chem. Lett.*, 2017, **8**, 4386–4390.

39 K.-K. Guo, M. Xu, Y. Zheng, X.-X. Wang, F.-Y. Li, W.-J. Xu and L. Xu, Exploring the Coordination Modes of a Keggin-Type $[ZnW_{12}O_{40}]^{6-}$ Anionic Cluster: Bonding Patterns, Crystal Structure, and Semiconducting Properties, *Inorg. Chem.*, 2021, **60**, 9097–9109.

40 P. Zhang, H. Li, Y. Wang, J. Song, J. Huang and P. Li, Highly efficient uranium(VI) remove from aqueous solution using nano-TiO_2-anchored polymerized dopamine-wrapped magnetic photocatalyst, *J. Cleaner Prod.*, 2023, **425**, 138796.

41 P. Liang, L. Yuan, H. Deng, X. Wang, L. Wang, Z. Li, S. Luo and W. Shi, Photocatalytic reduction of uranium(VI) by magnetic $ZnFe_2O_4$ under visible light, *Appl. Catal., B*, 2022, **267**, 118688.

42 J. He, Q. Han, J. Li, Z. Shi, X. Shi and J. Niu, Ternary supramolecular system for photocatalytic oxidation with air by consecutive photo-induced electron transfer processes, *J. Catal.*, 2019, **376**, 161–167.

43 X. Liu, R.-X. Bi, F.-T. Yu, C.-R. Zhang, Q.-X. Luo, R.-P. Liang and J.-D. Qiu, D-π-A array structure of $Bi_4Ti_3O_{12}$-triazine-aldehyde group benzene skeleton for enhanced photocatalytic uranium(VI) reduction, *J. Hazard. Mater.*, 2023, **451**, 131189.

